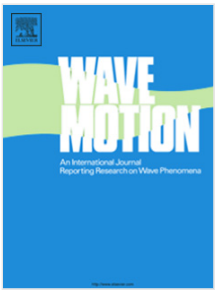

Generation of acoustic solitary waves in a lattice of Helmholtz resonators

Olivier Richoux, Bruno Lombard, Jean-François Mercier

PII: S0165-2125(15)00022-0
DOI: http://dx.doi.org/10.1016/j.wavemoti.2015.02.005
Reference: WAMOT 1917

To appear in: *Wave Motion*

Received date: 28 September 2014
Revised date: 3 February 2015
Accepted date: 16 February 2015

Please cite this article as: O. Richoux, B. Lombard, J.-F. Mercier, Generation of acoustic solitary waves in a lattice of Helmholtz resonators, *Wave Motion* (2015), http://dx.doi.org/10.1016/j.wavemoti.2015.02.005

***Research Highlights**

- Numerical modeling of nonlinear hyperbolic systems with nonlinear relaxation
- Experimental investigation of nonlinear propagation
- Validation of a theoretical model involving acoustic solitary waves

Generation of acoustic solitary waves in a lattice of Helmholtz resonators

Olivier Richoux[a,*], Bruno Lombard[b], Jean-François Mercier[c]

[a] *LAUM, UMR 6613 CNRS, Université du Maine, 72085 Le Mans, France*
[b] *LMA, CNRS, UPR 7051, Aix-Marseille Université, Centrale Marseille, 13402 Marseille, France*
[c] *POEMS, CNRS/ENSTA/INRIA, UMR 7231, ENSTA ParisTech, 91762 Palaiseau, France*

Abstract

This paper addresses the propagation of high amplitude acoustic pulses through a 1D lattice of Helmholtz resonators connected to a waveguide. Based on the model proposed by Sugimoto (J. Fluid. Mech., 244 (1992), 55-78), a new numerical method is developed to take into account both the nonlinear wave propagation and the different mechanisms of dissipation: the volume attenuation, the linear viscothermal losses at the walls, and the nonlinear absorption due to the acoustic jet formation in the resonator necks. Good agreement between numerical and experimental results is obtained, highlighting the crucial role of the nonlinear losses. Different kinds of solitary waves are observed experimentally with characteristics depending on the dispersion properties of the lattice.

Keywords: nonlinear acoustics, solitary waves, Helmholtz resonator, fractional derivatives, shock-capturing schemes

1. Introduction

The dynamics of nonlinear waves in lattices has been the object of a great interest in the scientific community. This theme has stimulated researches in

*Corresponding author
Email addresses: olivier.richoux@univ-lemans.fr (Olivier Richoux), lombard@lma.cnrs-mrs.fr (Bruno Lombard), jean-francois.mercier@ensta.fr (Jean-François Mercier)

a wide range of areas, including the theory of solitons and the dynamics of discrete networks. Works have been led in electromagnetism and optics [1], and numerous physical phenomena have been highlighted, such as dynamical multistability [2, 3, 4], chaotic phenomena [5, 6], discrete breathers [7, 8, 9] and solitons or solitary waves [10, 11]; for a review, see [12]. Solitary waves have been observed and studied firstly for surface wave in shallow water [13]. These waves can propagate without change of shape and with a velocity depending of their amplitude [14]. This phenomenon has been studied in many physical systems, for instance in fluid dynamics, optics, plasma physics. For a review, see [15] and the citations in [16].

In the field of acoustics, numerous works have shown the existence of solitary waves in uniform or inhomogeneous rods [17, 18, 19], periodic chains of elastics beads [20, 21, 22, 23, 24], periodic structures such as lattices or crystals [25, 26, 27], elastic layers [28, 29, 30], layered structures coated by film of soft material [31] and microstructured solids [32]. As we can see, most studies concern elastic waves in solids. Indeed, only a few works deal with acoustic waves in fluid, even if experimental observations of solitary waves have been made in the atmosphere [33, 34, 35] or in the ocean [36, 37, 38].

One reason of this lack originates from the fact that the intrinsic dispersion of acoustic equations is too low to compete with the nonlinear effects, preventing from the occurence of solitons. To observe the latter waves, geometrical dispersion must be introduced. It has been the object of the works of Sugimoto and his co-authors [39, 40, 41, 42], where the propagation of nonlinear waves was considered in a tube connected to an array of Helmholtz resonators. A model incorporating both the nonlinear wave propagation in the tube and the nonlinear oscillations in the resonators has been proposed. Theoretical and experimental investigations have shown the existence of acoustic solitary waves [39].

The present study extends the work of Sugimoto. We examine the validity of his theoretical model to describe the propagation of nonlinear acoustic waves in a tunnel with Helmholtz resonators. For this purpose, we develop both a new numerical method and real experiments. Compared with our original methodology presented in [43], improvements are introduced to model numerically the attenuation mechanisms. The combination of highly-accurate numerical simulations and experimental results enables to study quantitatively the generation of solitary waves, and also to determine the role of the different physical phenomena (such as the linear and nonlinear losses) on wave properties.

The paper is organized as follows. Section 2 introduces the model of Sugimoto [42]. Section 3 presents the evolution equations. The nonlocal fractional derivatives modeling the viscothermal losses are transformed into a set of memory variables satisfying local-in-time ordinary differential equations. Sugimoto's model is then transformed into a first-order system of partial differential equations. Section 4 details the numerical methods. The coefficients of the memory variables are issued from a new optimization procedure, which ensures the decrease of energy. A splitting strategy is then followed to integrate the evolution equations. Compared with [43], another novelty concerns the integration of a nonlinear differential equation describing the nonlinear losses. Section 5 introduces the experimental setup, the acquisition chain, and some validation tests. Section 6 compares the experimental results and the simulated results, confirming the validity of the theoretical model [40] and the existence of acoustic solitary waves.

2. Problem statement

2.1. Configuration

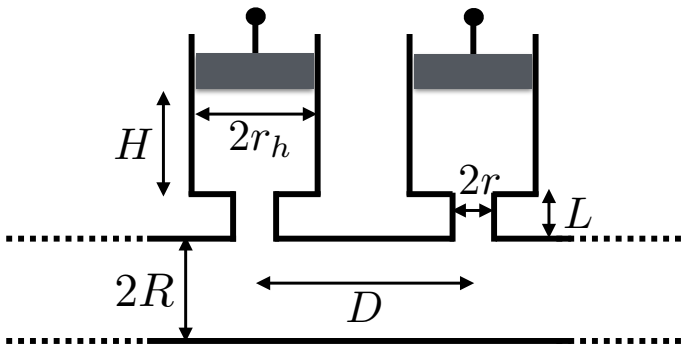

Figure 1: Sketch of the guide connected with Helmholtz resonators.

The configuration under study is made up of an air-filled tube connected with uniformly distributed cylindrical Helmholtz resonators (figure 1). The geometrical parameters are the radius of the guide R; the axial spacing between resonators D; the radius of the neck r; the length of the neck L; the

radius of the cavity r_h; and the height of the cavity H. The cross-sectional area of the guide is $A = \pi R^2$ and that of the neck is $B = \pi r^2$, the volume of each resonator is $V = \pi r_h^2 H$. Corrected lengths are introduced: $L^{'} = L + 2r$ accounts for the viscous end corrections, and the corrected length $L_e = L + \eta$ accounts for the end corrections at both ends of the neck, where $\eta \approx 0.82 r$ is determined experimentally [40]. The reduced radius is:

$$R^* = \frac{R}{1 - \frac{R}{2D}\frac{B}{A}} = \frac{R}{1 - \frac{r^2}{2DR}}. \tag{1}$$

The physical parameters are the ratio of specific heats at constant pressure and volume γ; the pressure at equilibrium p_0; the density at equilibrium ρ_0; the Prandtl number Pr; the kinematic viscosity ν; and the ratio of shear and bulk viscosities μ_v/μ. The linear sound speed a_0, the sound diffusivity ν_d, the dissipation in the boundary layer C, and the characteristic angular frequencies of the resonator ω_0 and ω_e, are given by:

$$\begin{aligned} &a_0 = \sqrt{\frac{\gamma p_0}{\rho_0}}, \qquad \nu_d = \nu\left(\frac{4}{3} + \frac{\mu_v}{\mu} + \frac{\gamma - 1}{\mathrm{Pr}}\right), \qquad C = 1 + \frac{\gamma - 1}{\sqrt{\mathrm{Pr}}}, \\ &\omega_0 = a_0\sqrt{\frac{B}{LV}} = a_0\frac{r}{r_h}\frac{1}{\sqrt{LH}}, \qquad \omega_e = \sqrt{\frac{L}{L_e}}\,\omega_0. \end{aligned} \tag{2}$$

2.2. Model of Sugimoto

Given a characteristic angular frequency ω, the main assumptions underlying Sugimoto's model are [40]:

- low-frequency propagation ($\omega < \omega^* = \frac{1.84\,a_0}{R}$), so that only the plane mode propagates and the 1D approximation is valid [44];
- weak acoustic nonlinearity in the tube (small Mach number) [45];
- continuous distribution of resonators ($\lambda \gg D$, where $\lambda = 2\pi a_0/\omega$).

The wave fields are split into simple right-going waves (denoted +) and left-going waves (denoted -) that do not interact together during their propagation. The variables are the axial velocity of the gas $u^{\pm}$ and the excess pressure in the cavity $p^{\pm}$. The excess pressure in the tube is denoted by $p^{'\pm}$. In the linear theory, it is related to $u^{\pm}$ by

$$p^{'\pm} = \pm\rho_0\, a_0\, u^{\pm}. \tag{3}$$

Each simple wave is modeled by a coupled system of a partial differential equation (PDE) and a ordinary differential equation (ODE):

$$\begin{cases} \dfrac{\partial u^{\pm}}{\partial t} + \dfrac{\partial}{\partial x}\left(\pm a u^{\pm} + b\dfrac{(u^{\pm})^2}{2}\right) = \pm c\dfrac{\partial^{-1/2}}{\partial t^{-1/2}}\dfrac{\partial u^{\pm}}{\partial x} + d\dfrac{\partial^2 u^{\pm}}{\partial x^2} \mp e\dfrac{\partial p^{\pm}}{\partial t}, & \text{(4a)} \\ \dfrac{\partial^2 p^{\pm}}{\partial t^2} + f\dfrac{\partial^{3/2} p^{\pm}}{\partial t^{3/2}} + g p^{\pm} - m\dfrac{\partial^2 (p^{\pm})^2}{\partial t^2} + n\left|\dfrac{\partial p^{\pm}}{\partial t}\right|\dfrac{\partial p^{\pm}}{\partial t} = \pm h u^{\pm}, & \text{(4b)} \end{cases}$$

with the coefficients

$$\begin{aligned} &a = a_0, \quad b = \frac{\gamma+1}{2}, \quad c = \frac{C\,a_0\sqrt{\nu}}{R^*}, \quad d = \frac{\nu_d}{2}, \quad e = \frac{V}{2\,\rho_0\,a_0\,A\,D}, \\ &f = \frac{2\sqrt{\nu}}{r}\frac{L^{'}}{L_e}, \quad g = \omega_e^2, \quad h = \omega_e^2\frac{\gamma\,p_0}{a_0}, \quad m = \frac{\gamma-1}{2\,\gamma\,p_0}, \quad n = \frac{V}{B\,L_e\,\rho_0\,a_0^2}. \end{aligned} \tag{5}$$

The PDE (4a) models nonlinear acoustic waves in the tube (coefficients a and b). Viscothermal losses in the boundary layer of the tube are introduced by the coefficient c [46]. The diffusivity of sound in the tube is also introduced by the coefficient d.

The ODE (4b) models the air oscillation in the neck of the resonators thanks to the coefficients f and g [47, 48]. Compared to the ODE used in [43], the following modifications have been introduced:

- the natural angular frequency of the resonator ω_0 has been replaced by the corrected angular frequency ω_e (2),
- f has been multiplied by $L^{'}/L_e$,
- new coefficients m and n have been introduced, describing nonlinear processes in the resonators.

The coefficient m models the nonlinearity due to the adiabatic process in the cavity. This term is conservative. The semi-empirical coefficient n accounts for the jet loss resulting from the difference in inflow and outflow patterns [40, 42]. As it will be illustrated later, these nonlinear processes need to be included to get good agreement with the experimental measurements.

The coupling between (4a) and (4b) is done by the coefficients e and h. If the resonators are suppressed ($H \to 0$ and thus $V \to 0$), then the coefficient $e \to 0$: no coupling occurs, and the classical Chester's equation is recovered [49].

Fractional operators of order -1/2 and 3/2 are involved in the system (4), via the coefficients c and f. These operators model the viscothermal losses in the tube and in the resonators, respectively proportional to $1/(i\,\omega)^{1/2}$ and $(i\,\omega)^{3/2}$ in the frequency domain. In (4a), the Riemann-Liouville fractional integral of order 1/2 of a causal function $w(t)$ is defined by

$$\frac{\partial^{-1/2}}{\partial t^{-1/2}} w(t) = \frac{H(t)}{\sqrt{\pi\, t}} * w = \frac{1}{\sqrt{\pi}} \int_0^t (t-\tau)^{-1/2} w(\tau)\, d\tau, \tag{6}$$

where * is the convolution product in time, and $H(t)$ is the Heaviside step function [50]. The Caputo fractional derivative of order 3/2 in (4b) is obtained by applying (6) to $\partial^2 p^{\pm}/\partial t^2$.

2.3. Dispersion regimes

Sugimoto's model (4) relies on a low-frequency assumption. In this case, the set of discrete Helmholtz resonators separated by portions of tube are replaced by a continuous surfacic distribution of resonators. To examine the validity of this model in our experimental configuration, one can compare the dispersion relations obtained respectively by the continuous model and by the discrete one, the latter being deduced from a Floquet-Bloch analysis [51].

In the linear regime, the lossy continuous model proposed by Sugimoto leads to the following dispersion relation [51]:

$$(QD)^2 = \left(1 - \sqrt{2}\,(1-i)\,\frac{C}{R^*}\left(\frac{\nu}{\omega}\right)^{1/2} + i\frac{\nu_d\,\omega}{a_0^2}\right)^{-1} \left(1 - \frac{\kappa}{Z_2(\omega)}\right) \left(\frac{\omega D}{a_0}\right)^2, \tag{7}$$

where Q is the Bloch wave number, $\kappa = V/(AD)$ and

$$Z_2(\omega) = \left(\frac{\omega}{\omega_e}\right)^2 - 1 + \frac{\sqrt{2}\,(1-i)}{r}\,\frac{L'}{L_e}\left(\frac{\nu}{\omega_e}\right)^{1/2}\left(\frac{\omega}{\omega_e}\right)^{3/2}.$$

On the contrary, the dispersion relation of the discrete model writes [52]

$$\cos QD = \cos(kD) + \frac{U(k)}{2k}\sin(kD), \tag{8}$$

where $k = \omega/a_0$ is the wave number and $U(k)$ is the equivalent potential of the Helmholtz resonators given by

$$U(k) = \frac{B}{A\,k}\,\frac{\tan(k\,L_e) + \alpha\tan(kH)}{1 - \alpha\tan(kL_e)\tan(kH)}, \tag{9}$$

with $\alpha = (r_h/r)^2$. The losses in the waveguide and resonators are modeled by introducing an imaginary part in the wavenumber k as presented in [51]. Results from equations (7) and (8) will be compared in section 5.3.

3. Evolution equations

3.1. Diffusive approximation

The fractional integral (6) is non local in time and relies on the full history of $w(t)$, which is numerically memory-consuming. An alternative approach is based on a diffusive representation of fractional derivatives, and then on its approximation. This method has already been presented in [43] and we just recall the main steps: following [53], equation (6) is recast as

$$\frac{\partial^{-1/2}}{\partial t^{-1/2}} w(t) = \int_0^{+\infty} \phi(t,\theta)\, d\theta, \tag{10}$$

where the diffusive variable ϕ satisfies the local-in-time ordinary differential equation

$$\begin{cases} \dfrac{\partial \phi}{\partial t} = -\theta^2\, \phi + \dfrac{2}{\pi}\, w, \\ \phi(0,\theta) = 0. \end{cases} \tag{11}$$

To approximate the integral (10), a quadrature formula on N_q points is used, with weights μ_ℓ and nodes θ_ℓ:

$$\frac{\partial^{-1/2}}{\partial t^{-1/2}} w(t) \simeq \sum_{\ell=1}^{N_q} \mu_\ell\, \phi_\ell(t), \tag{12}$$

where the diffusive variables $\phi_\ell(t) = \phi(t,\theta_\ell)$ satisfy the ODE (11). Similarly, the derivative of order $3/2$ is written

$$\frac{\partial^{3/2}}{\partial t^{3/2}} w(t) \simeq \sum_{\ell=1}^{N_q} \mu_\ell \left(-\theta_\ell^2\, \xi_\ell + \frac{2}{\pi}\, \frac{dw}{dt} \right), \tag{13}$$

where the $\xi_\ell(t) = \xi(t,\theta_\ell)$ satisfy the ODE

$$\begin{cases} \dfrac{\partial \xi}{\partial t} = -\theta^2\, \xi + \dfrac{2}{\pi}\, \dfrac{dw}{dt}, \\ \xi(0,\theta) = 0. \end{cases} \tag{14}$$

The determination of weights and nodes μ_ℓ and θ_ℓ is discussed in section 4.1.

3.2. First-order systems

Equations (4), (12), (11), (13) and (14) governing the evolution of right-going and left-going simple waves are put together. One obtains two first-order systems

$$\begin{cases} \dfrac{\partial u^\pm}{\partial t} + \dfrac{\partial}{\partial x}\left(\pm a u^\pm + b\dfrac{(u^\pm)^2}{2}\right) = \pm c \displaystyle\sum_{\ell=1}^{N_q} \mu_\ell\, \phi_\ell^\pm + d\frac{\partial^2 u}{\partial x^2} \mp e q^\pm, \\ \dfrac{\partial p^\pm}{\partial t} = q^\pm, \\ \dfrac{\partial q^\pm}{\partial t} = \dfrac{1}{1-2mp^\pm}\left(\pm h u^\pm - g p^\pm - f\displaystyle\sum_{\ell=1}^{N_q}\mu_\ell\left(-\theta_\ell^2\,\xi_\ell^\pm + \frac{2}{\pi}\,q^\pm\right) + 2m(q^\pm)^2 - n|q^\pm|\,q^\pm\right), \\ \dfrac{\partial \phi_\ell^\pm}{\partial t} - \dfrac{2}{\pi}\dfrac{\partial u^\pm}{\partial x} = -\theta_\ell^2\,\phi_\ell^\pm, \qquad \ell = 1\cdots N_q, \\ \dfrac{\partial \xi_\ell^\pm}{\partial t} = -\theta_\ell^2\,\xi_\ell^\pm + \dfrac{2}{\pi}\,q^\pm, \qquad \ell = 1\cdots N_q, \end{cases} \tag{15}$$

with null initial conditions. A source term at $x = 0$ models the acoustic source of right-going wave

$$u^+(0,t) = s(t). \tag{16}$$

The rigid end of the tube is modeled by Dirichlet conditions on the velocity

$$u^-(L,t) = -u^+(L,t), \tag{17}$$

hence $u^+(L,t)$ acts as a source for the system of left-going waves. In the third equation of (15), a division by $1-2mp^\pm$ occurs. In practice, this terms does not vanish: in the low-frequency regime, one has from (4b) that $gp^\pm \approx hu^\pm$ which leads to $p^\pm/p_0 \approx \gamma u^\pm/a_0$. From the definition of m in (5), it follows that

$$2mp^\pm \approx (\gamma-1)\,\frac{u^\pm}{a_0}, \tag{18}$$

which is lower than 1 under the hypothesis of weak nonlinearity ($|u^\pm| \ll a_0$).

The $(3+2\,N_q)$ unknowns for each simple waves are gathered in the two vectors

$$\mathbf{U}^\pm = \left(u^\pm,\, p^\pm,\, q^\pm, \phi_1^\pm, \cdots,\, \phi_{N_q}^\pm,\, \xi_1^\pm, \cdots,\, \xi_{N_q}^\pm\right)^T. \tag{19}$$

Then the nonlinear systems (15) can be written in the form

$$\frac{\partial}{\partial t}\mathbf{U}^{\pm} + \frac{\partial}{\partial x}\mathbf{F}^{\pm}(\mathbf{U}^{\pm}) = \mathbf{G}\,\frac{\partial^2}{\partial x^2}\mathbf{U}^{\pm} + \mathbf{S}^{\pm}(\mathbf{U}^{\pm}), \tag{20}$$

where $\mathbf{F}^{\pm}$ are the flux functions

$$\mathbf{F}^{\pm} = \left(\pm a u^{\pm} + b\,\frac{(u^{\pm})^2}{2},\, 0,\, 0,\, -\frac{2}{\pi}u^{\pm},\cdots,\, -\frac{2}{\pi}u^{\pm},\, 0,\cdots,\, 0\right)^T. \tag{21}$$

The Jacobian matrices $\frac{\partial \mathbf{F}^{\pm}}{\partial \mathbf{U}^{\pm}}$ in (21) are diagonalizable with real eigenvalues: $\pm a + b\,u^{\pm}$, and 0 with multiplicity $2\,N_q + 2$, which ensures propagation with finite velocity. These eigenvalues do not depend on the quadrature coefficients μ_ℓ and θ_ℓ. The diagonal matrix $\mathbf{G} = \mathrm{diag}(d,\, 0, \cdots,\, 0)$ incorporates the volume attenuation. Lastly, $\mathbf{S}^{\pm}$ are the source terms

$$\mathbf{S}^{\pm} = \begin{pmatrix} \pm c \sum_{\ell=1}^{N} \mu_\ell\, \phi_\ell^{\pm} \mp e\, q^{\pm} \\ q^{\pm} \\ \dfrac{1}{1-2mp^{\pm}}\left(\pm h u^{\pm} - g p^{\pm} - f \sum_{\ell=1}^{N} \mu_\ell \left(-\theta_\ell^2\, \xi_\ell^{\pm} + \dfrac{2}{\pi}\, q^{\pm}\right) + 2m(q^{\pm})^2 - n|q^{\pm}|q^{\pm}\right) \\ -\theta_\ell^2\, \phi_\ell^{\pm}, \qquad \ell = 1 \cdots N_q \\ -\theta_\ell^2\, \xi_\ell + \dfrac{2}{\pi}\, q^{\pm}, \qquad \ell = 1 \cdots N_q \end{pmatrix}. \tag{22}$$

As soon as $m \neq 0$ and $n \neq 0$, $\mathbf{S}^{\pm}(\mathbf{U}^{\pm})$ is no longer a linear operator ($m =$

$0 = n$ has been considered in [43]). The Jacobian matrices $\mathbf{T}^{\pm} = \frac{\partial \mathbf{S}^{\pm}}{\partial \mathbf{U}^{\pm}}$ are

$$\mathbf{T}^{\pm} = \begin{pmatrix} 0 & 0 & \mp e & \pm c\,\mu_1 & \cdots & \pm c\,\mu_N & 0 & \cdots & 0 \\ 0 & 0 & 1 & 0 & \cdots & 0 & 0 & \cdots & 0 \\ \dfrac{\pm h}{\Delta^{\pm}} & -\dfrac{g}{(\Delta^{\pm})^2} & T_{22}^{\pm} & 0 & \cdots & 0 & \dfrac{f}{\Delta^{\pm}}\,\mu_1\,\theta_1^2 & \cdots & \dfrac{f}{\Delta^{\pm}}\,\mu_N\,\theta_N^2 \\ 0 & 0 & 0 & -\theta_1^2 & & & & & \\ \vdots & \vdots & \vdots & & \ddots & & & & \\ 0 & 0 & 0 & & & -\theta_N^2 & & & \\ 0 & 0 & \dfrac{2}{\pi} & & & & -\theta_1^2 & & \\ \vdots & \vdots & \vdots & & & & & \ddots & \\ 0 & 0 & \dfrac{2}{\pi} & & & & & & -\theta_N^2 \end{pmatrix}, \tag{23}$$

with

$$\Delta^{\pm} = 1 - 2mp^{\pm}, \qquad T_{22}^{\pm} = \frac{1}{\Delta^{\pm}}\left(4mq^{\pm} - 2n|q^{\pm}| - \frac{2}{\pi} f \sum_{\ell=1}^{N_q} \mu_\ell\right). \tag{24}$$

4. Numerical methods

4.1. Quadrature coefficients

In [43], a detailed discussion on the possible strategies to compute the $2\,N_q$ quadrature coefficients μ_ℓ and θ_ℓ in (22) has been proposed, and a linear optimization was preferred. The nodes θ_ℓ were distributed linearly on a logarithmic scale on the frequency range of interest, and then the weights were determined by a simple least-squares method. One drawback is that negative weights μ_ℓ may be obtained, which may yield a non-physical increase of energy [54].

Here we improve the optimization procedure to get positive weights μ_ℓ. Applying Fourier transforms in time and space to the original model of Sugimoto (4) and to its diffusive counterpart (15), we obtain two dispersion relations. The latters differ only in the symbols

$$\begin{cases} \chi(\omega) = (i\,\omega)^{-1/2}, \\ \tilde{\chi}(\omega) = \dfrac{2}{\pi} \displaystyle\sum_{\ell=1}^{N_q} \frac{\mu_\ell}{\theta_\ell^2 + i\,\omega}. \end{cases} \tag{25}$$

For a given number K_q of angular frequencies ω_k, one introduces the objective function

$$\mathcal{J}\left(\{(\mu_\ell,\theta_\ell)\}_\ell\,;N_q,K_q\right)=\sum_{k=1}^{K_q}\left|\frac{\tilde{\chi}(\omega_k)}{\chi(\omega_k)}-1\right|^2=\sum_{k=1}^{K_q}\left|\frac{2}{\pi}\sum_{\ell=1}^{N_q}\mu_\ell\,\frac{(i\omega_k)^{1/2}}{\theta_\ell^2+i\omega_k}-1\right|^2 \tag{26}$$

to be minimized w.r.t parameters $\{(\mu_\ell,\theta_\ell)\}_\ell$ for $\ell=1,\ldots,N_q$. A nonlinear optimization with the positivity constraints $\mu_\ell\geq 0$ and $\theta_\ell\geq 0$ is chosen for this purpose. The additional constraint $\theta_\ell\leq\theta_{\max}$ is also introduced to avoid the algorithm to diverge. These $3N_q$ constraints can be relaxed by setting $\mu_\ell=\mu_\ell^{'2}$ and $\theta_\ell=\theta_\ell^{'2}$ and solving the following problem with only N_q constraints

$$\min_{\{(\theta'_\ell,\mu'_\ell)\}_\ell}\ \mathcal{J}\left(\{(\mu_\ell^{'2},\theta_\ell^{'2})\}_\ell\,;N_q,K_q\right)\qquad\text{with }\theta_\ell^{'2}\leq\theta_{\max}\text{ for }\ell=1,\ldots,N_q. \tag{27}$$

As problem (27) is nonlinear and non-quadratic w.r.t. nodes θ'_ℓ, we implement the algorithm SolvOpt [55, 56] based on the iterative Shor's method [57]. Initial values used in the algorithm must be chosen with care; for this purpose we propose to use the coefficients obtained by the modified Jacobi approach [58]: see method 3 of [43]. Finally, the angular frequencies ω_k for $k=1,...,K_q$ in (26) are chosen linearly on a logarithmic scale over a given optimization band $[\omega_{\min},\omega_{\max}]$, i.e.

$$\omega_k=\omega_{\min}\left(\frac{\omega_{\max}}{\omega_{\min}}\right)^{\frac{k-1}{K_q-1}}. \tag{28}$$

The choice of $\omega_{\min}$ and $\omega_{\max}$ depends on the configuration under study (tube alone or coupled system with resonators) and has been detailed in [43]. Besides the positivity of the quadrature coefficients, a great improvement of accuracy is observed numerically when using the nonlinear optimization described above.

4.2. Numerical scheme

In order to integrate the systems (20), a grid is introduced with a uniform spatial mesh size $\Delta x=L/N_x$ and a variable time step Δt_n. The approximation of the exact solution $\mathbf{U}^{\pm}(x_j=j\,\Delta x,t_n=t_{n-1}+\Delta t_{n-1})$ is denoted by $\mathbf{U}_j^{n\pm}$. A splitting strategy is followed here, ensuring both simplicity and

efficiency. Instead of integrating the original equations (20), propagative equations

$$\frac{\partial}{\partial t}\mathbf{U}^{\pm} + \frac{\partial}{\partial x}\mathbf{F}^{\pm}(\mathbf{U}^{\pm}) = \mathbf{G}\,\frac{\partial^2}{\partial x^2}\mathbf{U}^{\pm} \tag{29}$$

and forcing equations

$$\frac{\partial}{\partial t}\mathbf{U}^{\pm} = \mathbf{S}^{\pm}\left(\mathbf{U}^{\pm}\right) \tag{30}$$

are solved successively. The discrete operators to solve (29) and (30) are denoted by $\mathbf{H}_a^{\pm}$ and $\mathbf{H}_b^{\pm}$, respectively. Strang splitting [59] is then used between t_n and t_{n+1}, solving successively (29) and (30) with adequate time increments:

$$\begin{aligned}
&\bullet\ \mathbf{U}_j^{(1)\pm} &&= \mathbf{H}_b^{\pm}(\tfrac{\Delta t_n}{2})\,\mathbf{U}_j^{n\pm},\\
&\bullet\ \mathbf{U}_j^{(2)\pm} &&= \mathbf{H}_a^{\pm}(\Delta t_n)\,\mathbf{U}_j^{(1)\pm},\\
&\bullet\ \mathbf{U}_j^{(n+1)\pm} &&= \mathbf{H}_b^{\pm}(\tfrac{\Delta t_n}{2})\,\mathbf{U}_j^{(2)\pm}.
\end{aligned} \tag{31}$$

Provided that $\mathbf{H}_a^{\pm}$ and $\mathbf{H}_b^{\pm}$ are second-order accurate and stable operators, the time-marching (31) gives second-order accurate approximations of the original equations (20).

As explained in [43], the propagative equation (29) is solved by a standard second-order TVD scheme for nonlinear hyperbolic PDE [60] combined with a centered finite-difference approximation. The discrete operator $\mathbf{H}_a$ is stable under a usual CFL condition.

Contrary to [43] where $\mathbf{S}^{\pm}$ was a constant linear operator, the forcing equations (30) can no longer be solved exactly. Here, they are solved by a second-order implicit trapezoidal method [59]

$$\mathbf{U}^{(n+1)\pm} = \mathbf{U}^{n\pm} + \frac{\tau_n}{2}\left(\mathbf{S}^{\pm}(\mathbf{U}^{n\pm})) + \mathbf{S}^{\pm}(\mathbf{U}^{(n+1)\pm})\right), \tag{32}$$

with $\tau_n = \Delta t_n/2$. The nonlinear systems (32) are solved iteratively by the Newton-Raphson method. In practice, a single iteration is accurate enough. Linearizing the equations and using the Jacobian (23), the discrete operator $\mathbf{H}_b^{\pm}$ recovers the semi-implicit trapezoidal scheme

$$\mathbf{U}^{(n+1)\pm} = \mathbf{U}^{n\pm} + \tau_n\left(\mathbf{I} - \frac{\tau_n}{2}\,\mathbf{T}^{n\pm}\right)^{-1}\mathbf{S}^{\pm}(\mathbf{U}^{n\pm}), \tag{33}$$

which is unconditionnally stable.

Once time-marching is completed, the source terms (16) and (17) are updated at the grid nodes 0 (for the right-going wave) and N_x (for the left-going wave). The forcing term $s(t_n)$ in (16) is obtained from (3) and from the pressure $p^{'}(0, t_n)$ measured experimentally by the first microphone: see section 5 for details on that topic.

5. Experimental set-up and validation

5.1. Lattice sample

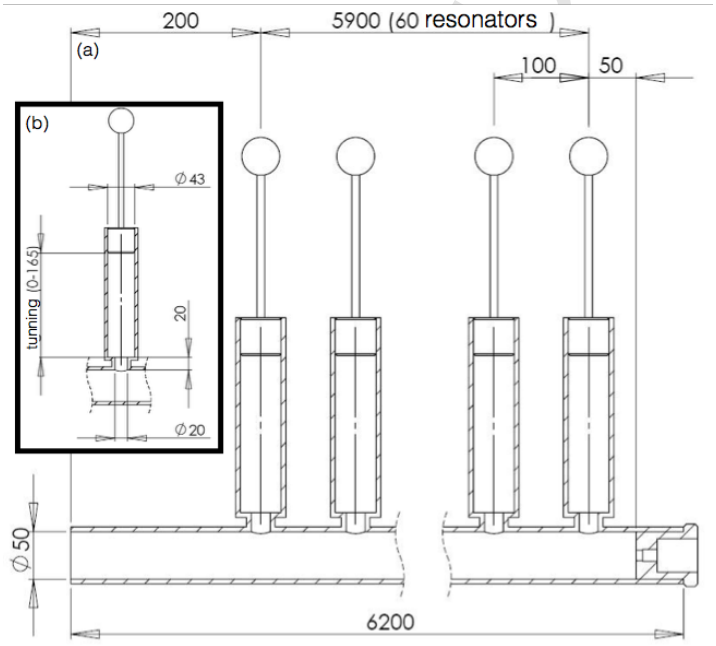

Figure 2: experimental set-up; all the dimensions are detailed in mm. (a): description of the Helmholtz resonators lattice. (b): description of one Helmholtz resonator.

The experimental set-up shown in figure 2-(a) consists in a 6.2 m long cylindrical waveguide connected to an array of 60 Helmholtz resonators periodically distributed. The position inside the waveguide is labeled using its

axis called x-axis. The origin of the x-axis, $x = 0$, is placed at the beginning of the main tube. All the cavities have the same height H, which may varies between 0 and $H_{max} = 0.165$ m, as described in figure 2-(b). The physical and geometrical parameters are given in table 1. The physical data correspond to air at 15 °C.

γ	p_0 (Pa)	ρ_0 (kg/m^3)	Pr	ν (m^2/s)	μ_v/μ
1.403	10^5	1.177	0.708	$1.57\,10^{-5}$	0.60
R (m)	D (m)	r (m)	L (m)	r_h (m)	H_{max} (m)
0.025	0.1	0.01	0.02	0.0215	0.165

Table 1: physical parameters of air at 15 °C, and geometrical data.

The first resonator lies 0.2 m after the beginning of the tube and its location is referred to as $x = 0.2$ m in the axis of the tube. The end of the lattice is closed by a rigid cork located at $D/2$ after the last resonator. Then, the waves impinging the lattice end are reflected and travel in the opposite direction (keeping the cell length constant) into the lattice, allowing to increase the lattice length from 6 m to 12 m. Numerical modeling of this configuration amounts to solve (4) by considering a 0.2 m long waveguide with no resonator, connected to a 5.95 m long lattice of resonators closed by a rigid end, in accordance with the experimental set-up.

A second experimental system, consisting in a waveguide with no array of resonator, is used in section 5.4 to highlight the influence of the Helmholtz resonators in the nonlinear process. This waveguide has exactly the same features as the previous one. Numerical modeling of this configuration amounts to solve (4a) on a 6.15 m long waveguide closed by a rigid end, with $e = 0$.

5.2. Source and acquisition

The input signal is generated by the explosion of a latex balloon (from a commercial store) with a spherical shape corresponding to a recommended diameter of 25 cm. The latter is introduced into a 20 cm long waveguide with diameter 5 cm closed at one end and connected to the entry of the main tube at the other end. Using an air pump, the balloon is inflated until its explosion. The shape of the generated impulsion (width and amplitude) depends on the balloon length at the explosion time, varying slightly from one experiment to another.

The excess pressure $p' = p'^{+} + p'^{-}$ is measured with 3 PCB 106B microphones. They are located at the beginning of the system (20 cm before the

first resonator) and at 2 different positions into the lattice, depending on the experiment. The sensibility of the microphones is 0.045 V/kPa, and a PCB 441A101 conditioning amplifier is used for each of them. The acquisition is made by a National Instrument BNC 2110 card with a sample frequency of 250 kHz, connected to a computer.

The input signal shown in the figure 3-(a) can be described by a gate-signal with a high amplitude around 30 kPa, and a width around 1.5 ms with the presence of a tail caused by reflexion at the end of the source tube. The initial excess pressure consists of a compression wave. The figure 3-(b) shows the spectrum of the input signal and points out that the frequency range excited by the source is mostly included in $[0 - 650]$ Hz. This input signal, generated by the balloon explosion, is measured at each experiment. It is then injected in the numerical scheme and acts as a forcing term s: see section 4.2. In other words, our resolution method requires only the input data signal as initial conditions to solve the system (4). It is an important difference with the resolution method in [42] which requires the fitting of the experimental signal after some distance of propagation.

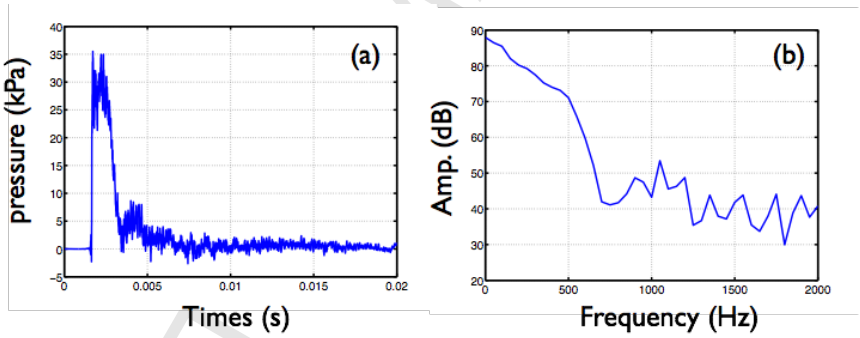

Figure 3: acoustic source measured at the entry of the tube. (a): time history of the excess pressure $p^+(0,t)$. (b): Fourier transform of the signal.

5.3. Linear dispersion in a Helmholtz resonator lattice

The goal of this section is to examine the validity of the model (4) to describe the experimental configuration under study. For this purpose, figure 4 compares the dispersion curves obtained with the continuous description of

resonators (7) and with the discrete description (8). Three different heights of resonators are considered: $H = 16.5$ cm ($f_0 = 345$ Hz), $H = 7$ cm ($f_0 = 586$ Hz), and $H = 2$ cm ($f_0 = 1027$ Hz). In each case, $f_0 = \omega_0/(2\pi)$ is the resonance frequency of the Helmholtz resonators (2).

Good agreement between these two families of dispersion curves is obtained on a large frequency domain, up to the Bragg band gap at 1800 Hz. Because of the continuous approximation, equation (7) cannot predict the Bragg band gap due to the lattice periodicity. However, the first hybridization band gap (due to Helmholtz resonance) is well described by the continuous model.

A second observation deduced from figure 4 concerns the dispersive behavior of the medium under study. Recall that the upper limit of the source frequency range $f_{\max}$ is around 650 Hz. If $f_0 \gg f_{\max}$ (i.e. $H = 2$ cm), we observe a linear frequency dependance of QD in $[0, f_{\max}]$, which implies that the dispersion is weak (figure 4-(c)). On the contrary, when f_0 lies in the source frequency range (figure 4-(a) for $H = 16.5$ cm and figure (4b) for $H = 7$ cm), the dispersion is strong. This impacts strongly the shape of the waves, as detailed in section 6.4.

5.4. Tube without resonators

Before considering the interaction of waves with the lattice of resonators, we consider the simple case of a uniform tube. Figure 5 shows the profiles of the measured and simulated excess pressure p'/p_s at the position $x = 6.15$ m in a waveguide without resonator, where p_s is the magnitude of the input signal. The blue and red lines correspond to the simulated and experimental results, respectively. The initial pressure wave has evolved to a triangular shape wave during the propagation, due to a well-known nonlinear process [45, 49].

The good agreement between the simulated and measured pressure highlights the validity of the lossy nonlinear model for the waveguide propagation described by the equation (4a) where the coupling term with the resonators is canceled. The model describing the losses in the waveguide propagation by fractional derivatives is verified by this comparison and will not be discussed further. Note lastly that the volume attenuation and the viscothermal losses in the tube are insufficient to prevent from the occurrence of shocks [61].

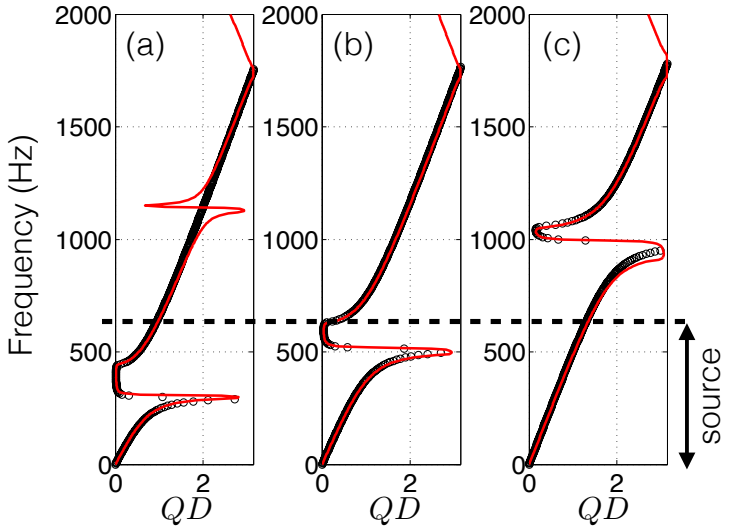

Figure 4: dispersion relation of an array of Helmholtz resonators for $H = 16.5$ cm (a), $H = 7$ cm (b) and $H = 2$ cm (c). The open circles correspond to the continuous model (7). The continuous red line corresponds to the discrete model (8).

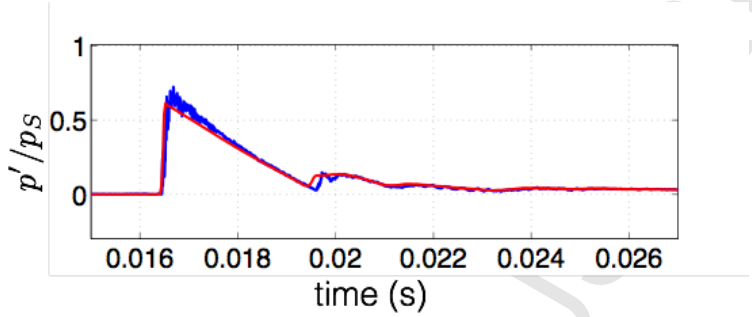

Figure 5: time history of the excess pressure p'/p_s in a tube with no array of resonators, at $x = 6.15$ m. The blue and red lines represent the experimental and simulated profiles, respectively.

6. Experiments in a tube with resonators

6.1. Existence of solitary waves

Figure 6 presents the experimental and simulated temporal profiles p'/p_s at $x = 2.1$ m, in a waveguide connected to an array of Helmholtz resonators. The heights of resonators are $H = 7$ cm (figure 6-(a)) and $H = 13$ cm (figure 6-(b)), respectively. In the case $H = 7$ cm (resp. $H = 13$ cm), the resonance frequency f_0 of the Helmholtz resonators is $f_0 \simeq 586$ Hz (resp. $f_0 \simeq 414$ Hz). The blue line depicts the experimental results. The red line depicts the numerical results where all the physical phenomena are incorporated, leading to the full system (4). The black line depicts the numerical solution obtained without incorporating the nonlinear processes in the resonators: $m = n = 0$ in (4b).

Unlike the waveguide without resonators, where a triangular wave is obtained (figure 5), the lattice produces a wave with a smooth and symmetrical shape (figure 6). This constitutes a signature of solitary waves.

Good agreement between experimental and simulated waves is obtained when the nonlinear terms in the resonators (essentially losses due to the term n in (4b)) are taken into account. On the contrary, the linear viscothermal losses alone are insufficient to predict the right amplitude, which is overestimated compared to the experimental results. Moreover, spurious oscillations are observed in the linear case, that are suppressed when nonlinear losses are

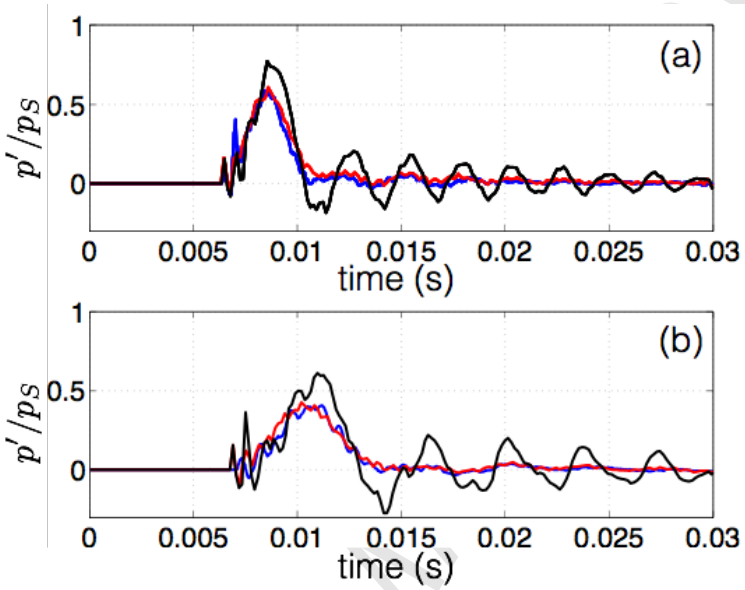

Figure 6: time history of the excess pressure p'/p_s at $x = 2.1$ m in a tube with an array of resonators. The heights of resonators are: $H = 7$ cm (a), $H = 13$ cm (b). The blue line represents the experimental pressure. The red and black lines represent the simulated pressure, with (red) or without (black) nonlinear losses.

incorporated.

In addition, the comparison between the heights $H = 7$ cm (figure 6-(a)) and $H = 13$ cm (figure 6-(b)) highlights the influence of the resonators on the evolution of the pulse. The solitary wave being the result of a competition between the nonlinearity and the dispersion in the media, it is very sensitive to the cavity length. The decrease of the Helmholtz resonance frequency leads to an increase of the wave attenuation, an increase of the pulse width, and a decrease of the wave celerity. These results corroborate the theoretical analysis performed in [42] and confirm the existence of an acoustic solitary wave.

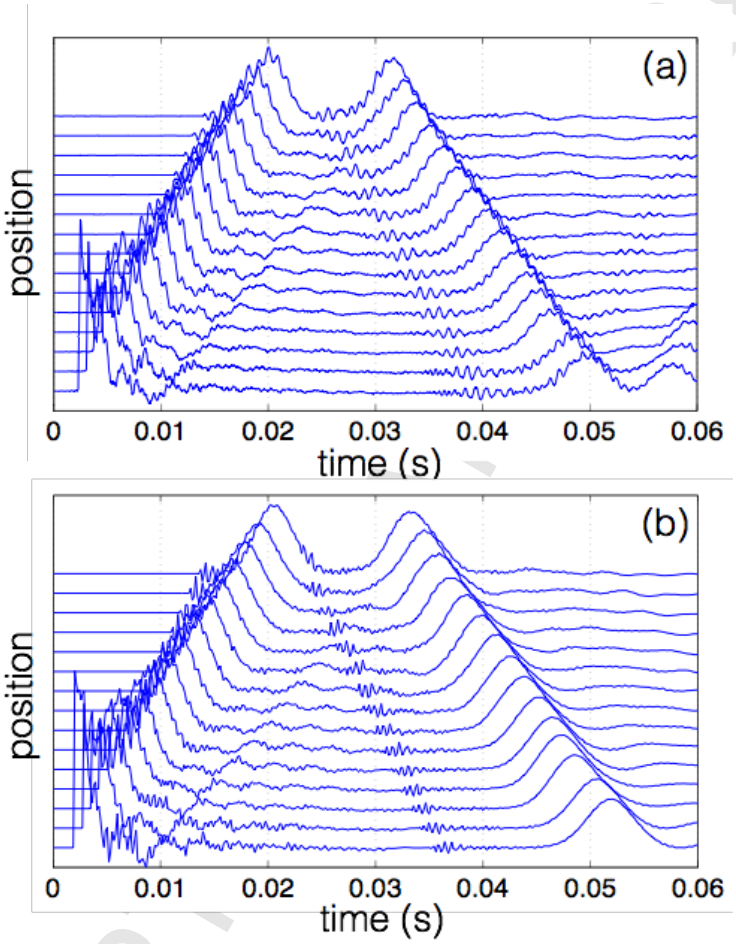

Figure 7: spatio-temporal evolution of the waves in a waveguide with an array of resonators of height $H = 13$ cm. (a) experiments, (b) simulations. The horizontal axis represents the time t.

6.2. Spatio-temporal evolution

In this section, we illustrate the evolution of solitary waves during their propagation, in the case $H = 13$ cm. Figure 7 displays the experimen-

tal results (top panel) and the simulated results with nonlinear attenuation (bottom panel), in the space × time plane.

Experimentally (figure 7-(a)), the signals have been recorded at 15 different positions of microphones regularly spaced, from 0.2 m to 4.4 m inside the lattice with a spacing 0.3 m. Since only two microphones were available, acquisition was performed during 8 successive experiments, the pair of microphones being successively shifted. A new source was used in each experiment, leading to small deviations from one experiment to the other. These 8 sources were used as initial data for the corresponding numerical simulations. For both experiments and simulations, we present the ratio between the excess pressure in the waveguide and the source amplitude p'/p_s.

Figure 7 clearly shows the propagation of a solitary wave without change of shape and with a constant velocity characterized by a constant slope in the space × time plane, both experimentally and numerically. The symmetry of figure 7 with respect to time $t = 29$ ms illustrates the reflexion of the solitary wave at the closed end of the tube. A second reflexion at the opposite closed end is visible in the experimental case, but it is not simulated numerically. The experimental and simulated results are in good agreement, for both the shape and the velocity of the waves.

6.3. Attenuation

Figure 8 illustrates the attenuation of acoustic solitary waves during their propagation, in the case of resonators with height $H = 13$ cm. Experimental results are shown in blue line, and simulated results are shown in red and black lines. The red line has been computed by incorporating all the nonlinear mechanisms in the resonator (in particular the nonlinear attenuation due to jet loss in the neck), whereas the black line incorporates only the linear viscothermal losses ($m = n = 0$ in (4b)). All these results are deduced from the experimental and simulated data presented in the previous section. Good agreement between experiments and simulations is obtained when the nonlinear absorption process is taken into account.

The evolution of the attenuation in terms of the distance highlights two regimes in the wave propagation: a strong attenuation during the first 2 meters (50 %), followed by a weaker attenuation during the remaining propagation. Two different mechanisms are involved in the attenuation process to explain this observation. Firstly, the nonlinear absorption taking place in the resonator necks is preponderant during the first meters, due to the high amplitude of the initial pulse, which leads to a strong decrease. We recall

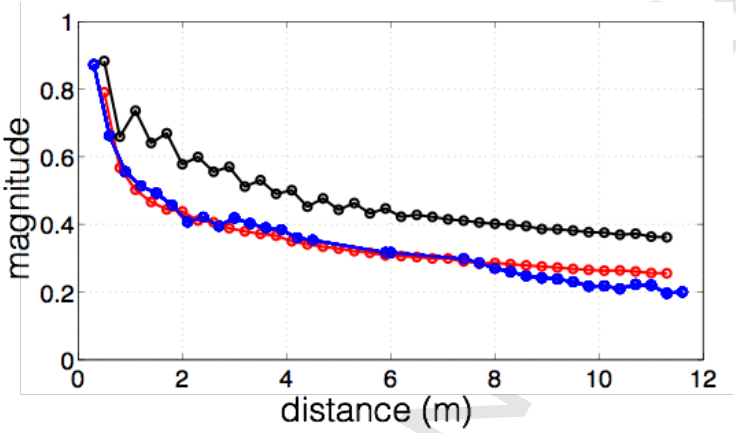

Figure 8: magnitude of the solitary wave in terms of the propagation distance in the lattice, with Helmholtz resonators of height $H = 13$ cm. Blue line presents the experimental results. Red and black lines present the numerical results obtained with the full model (red) and without the nonlinear attenuation (black).

here that the nonlinear absorption of the resonators is due to the jet loss resulting from the difference in inflow and outflow patterns. Secondly and owing to the weaker amplitude, the cumulative effects of linear viscothermal losses in the boundary layer of the tube during the propagation prevail, resulting in a lower attenuation. These mechanisms are deduced from the simulations without the nonlinear absorption: in the first regime, the attenuation is largely underestimated while for the second regime the slope of the decay is well found.

To highlight these two different regimes, figure 9 shows the time evolution of the wave recorded during the first 3 meters. The shape of the initial high amplitude pulse is greatly modified, leading to a symmetrical and smooth shape after 2 m of propagation. In addition, a strong attenuation is observed (50 % of amplitude decay). After, the wave shape remains constant and the attenuation becomes weaker. Again, these results show the crucial role of nonlinear absorption process in the evolution of a high amplitude pulse to a solitary wave.

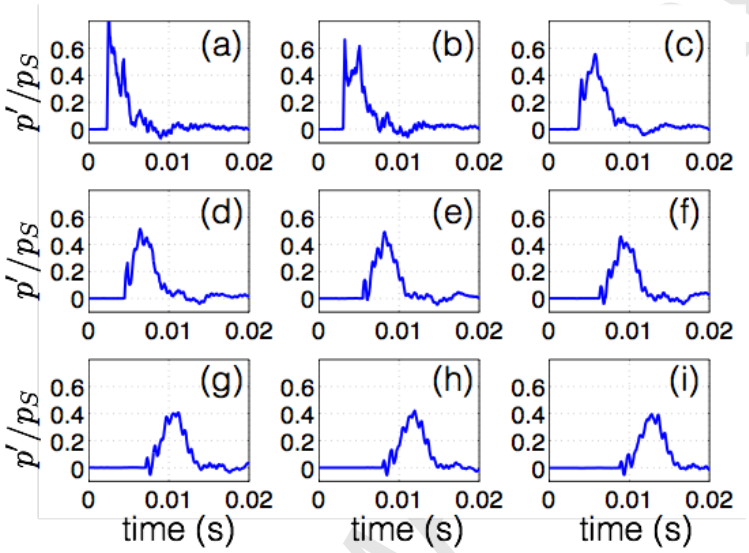

Figure 9: time history of the excess pressure p'/p_s measured experimentally in the case of Helmholtz resonators of height $H = 13$. The measures are done from $x = 0.2$ m to $x = 2.6$ m, with a spacing 0.3 m.

6.4. Influence of the dispersion

Here we study the influence of the Helmholtz resonance frequency on the features of the solitary waves (velocity, amplitude and shape). Experimental and simulated time evolutions of p'/p_s are compared in figure 10 in the case of heights $H = 2$ cm (figure 10-(a)) and $H = 16.5$ cm (figure 10-(b)). Three waves are observed from the left to the right, corresponding successively to the direct wave at the receivers $x = 2.8$ m and 5.95 m, and to the reflected wave at $x = 2.8$ m. In the case $H = 2$ cm ($f_0 = 1027$ Hz), the dispersion is weak in the frequency range of the source (see figure 4), contrary to the case $H = 16.5$ cm ($f_0 = 345$ Hz) where the dispersion is strong. Comparing these two cases shows the essential role of the dispersion on the characteristics of the wave.

Weak dispersion combined with nonlinear propagation (figure 10-(a)) leads to a narrow, compact and less attenuated solitary wave with a high

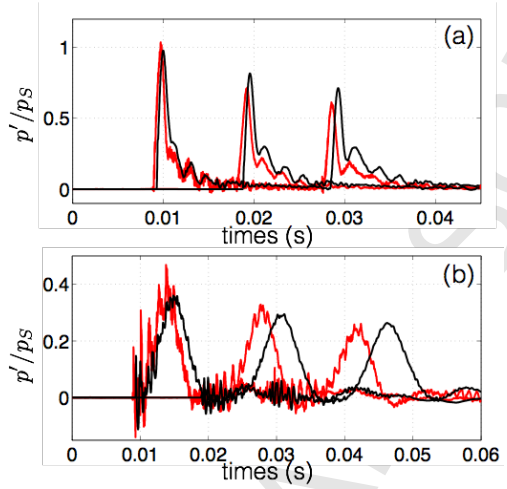

Figure 10: time history of the excess pressure p'/p_s at $x = 2.8$ m and $x = 5.95$ m. (a) $H = 2$ cm, corresponding to $f_0 = 1027$ Hz. (b) $H = 16.5$ cm, corresponding to $f_0 = 345$ Hz. Experimental and numerical results are shown in red line and black line, respectively.

velocity. In this case, the velocity and the shape are well recovered by the simulation. For strong dispersion (figure 10-(b)), the wave is more attenuated and its shape becomes larger. The simulated half-width and the amplitude of the wave are in good agreement with the experimental ones. However, a slight shift of the positions of waves is observed.

A systematic study is then performed by considering six cavity heights: $H = 2, 3, 7, 10, 13, 16.5$ cm. The experimental and simulated excess pressure $p^{'}$ is measured at $x = 2.8$ m and 5.95 m in the lattice. The velocity is deduced from the traveltime of the maximum of the wave. The attenuation factor is given by the ratio of the maximum amplitudes at the two receivers. The shape is characterized by the half-width of the solitary wave at $x = 5.95$ m.

All the results are displayed in the figure 11-(a,b,c), where the experimental results and the numerical results are shown in red and black line, respectively. Experiments and simulations are in good agreement, denoting the good description of the physics by the model and the efficiency of the numerical method. As expected, the features of the solitary wave are

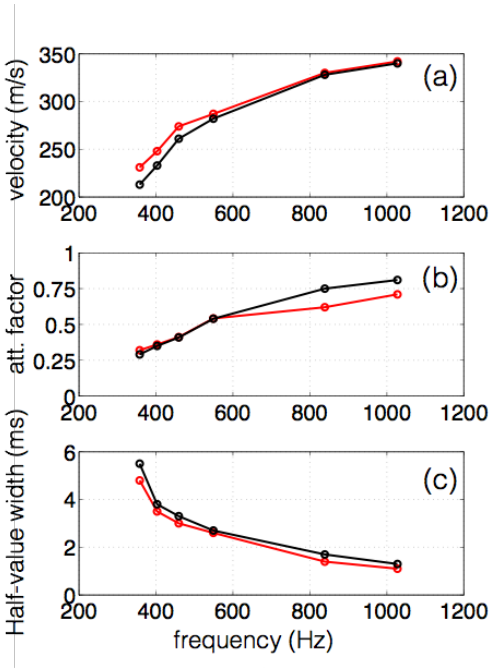

Figure 11: (a) velocity, (b) attenuation factor and (c) half-width of the pulse versus resonance frequencies of the resonators. Experimental and numerical results are shown in red line and black line, respectively.

highly dependent on the Helmholtz resonance frequencies. High resonance frequency (small H) yields large velocity, low attenuation (attenuation factor close to 1) and narrow wave. The velocity of the wave is close to the sound speed. For low resonance frequency, conversely, the velocity decreases and the attenuation and the width of the wave increases. These observations confirm the main properties of the solitary waves, theoretically analyzed in [41].

7. Conclusion

We have studied numerically and experimentally the propagation of high amplitude pulses in a lattice of Helmholtz resonators. We have proposed a new time-domain numerical method to describe the linear viscothermal losses in the waveguide and the nonlinear absorption due to the acoustic jet formation in the necks of resonators. The comparisons between numerical and experimental results has validated the theoretical model (4) proposed by Sugimoto, as long as the dissipation processes are correctly incorporated. Two different regimes of propagation have been observed. Firstly, a strong attenuation regime, dominated by the nonlinear absorption process, reduces largely the amplitude of waves and reshapes the acoustic pulses to generate a solitary wave. Secondly, linear losses in the waveguide produce a lower mitigation of the solitary wave leading to an almost-constant shape.

The properties of the acoustic solitary waves have been studied in terms of the dispersion of the lattice. In the case of low dispersion, the solitary wave is compact with a narrow shape. Its velocity is close to the sound celerity and its attenuation is weak. In the case of a strong dispersion, the shape of the solitary wave is broader, its velocity is smaller and its attenuation is large. The numerical and the experimental studies show the great importance of losses in the generation of acoustic solitary waves in periodic locally resonant structures. It contributes to promising research in the field of nonlinear acoustic propagation in metamaterials and acoustic transmission filters. Future works will be devoted to the study of nonlinear acoustic propagation in disordered systems. In particular, our numerical and experimental set-ups will be used to investigate the competition between nonlinear dynamics, dispersion processes and disorder effects.

Acknowledgments. This study has been supported by the Agence Nationale de la Recherche through the grant ANR ProCoMedia, project ANR-10-INTB-0914.

[1] P. G. Kevrekidis, Non-linear waves in lattices: past, present, future, IMA J. Appl. Math., 76-3 (2011), 389-423.

[2] Y. Wan, C. M. Soukoulis, Wave transmission in one-dimensional nonlinear lattice : multi stability and noise, Springer Proceedings in Physics: Disorder and Nonlinearity, 39, Springer-Verlag, Berlin (1989).

[3] P. Hawrylak, M. Grabowski, Self-induced gaps and optical bistability in semiconductor superlattices, Phys. Rev. B, 40-11 (1989), 8013–8016.

[4] Q. Li, C. T. Chan, K. M. Ho, C. M. Soukoulis, Wave propagation in nonlinear photonic band-gap materials, Phys. Rev. B, 53-23 (1996), 15577–1585.

[5] M. Grabowski, P. Hawrylak, Wave propagation in a nonlinear periodic medium, Phys. Rev. B, 41-9 (1990), 5783–5791.

[6] Y. Wan, C. M. Soukoulis, One-dimensional nonlinear Schrödinger equation: A nonlinear dynamical approach, Phys. Rev. A, 41-2 (1990), 800–809.

[7] N. Lazarides, M. Eleftheriou, G. P. Tsironis, Discrete breathers in nonlinear magnetic metamaterials, Phys. Rev. Lett., 97-15 (2006), 157406.

[8] N. Boechler, G. Theocharis, S. Job, P. G. Kevrekidis, M. A. Porter, C. Daraio, Discrete breathers in one-dimensional diatomic granular crystals, Phys. Rev. Lett., 104-24 (2010), 244302.

[9] B. F. Feng, T. Kawahara, Discrete breathers in two-dimensional nonlinear lattices, Wave Motion, 45-2 (2007), 68-82.

[10] Q. Li, C. M. Soukoulis, S. Pnevmatikos, E. N. Economou, Scattering properties of solitons in nonlinear disordered chains, Phys. Rev. B, 38-16 (1988), 11888–11891.

[11] Q. Li, S. Pnevmatikos, E. N. Economou, C. M. Soukoulis, Lattice-soliton scattering in nonlinear atomic chains, Phys. Rev. B, 37-7 (1988), 3534–3541.

[12] Y. V. Kartashov, B. A. Malomed, L. Torner, Solitons in Nonlinear Lattices, Rev. Mod. Phys., 83-1 (2011), 247-305.

[13] J. S. Russell, Report on Waves, Made to the Meetings of the British Association in 1842-1843, Report of the British Association for the Advancement of Science, John Murray, London (1844).

[14] M. Remoissenet, Waves Called Solitons: Concepts and Experiments, Springer-Verlag, New-York (1999).

[15] J. Engelbrecht, V. Fridman, E. Pelinovski, Nonlinear Evolution Equations, Longman, Harlow (1988).

[16] T. Dauxois, M. Peyrard, Physics of Solitons, Cambridge University Press (2006).

[17] H. H. Dai, Y. Huo, Solitary waves in an inhomogeneous rod composed of a general hyper elastic material, Wave Motion, 35 (2002), 55-69.

[18] K. R. Khusnutdinova, A. M. Samsonov, Fission of longitudinal strain solitary wave in a delaminated bar, Phys. Rev. E, 77-6 (2008), 06603.

[19] M. de Billy, A. C. Hladky-Hennion, Generation of transversal envelope soliton in polymeric and wooden rods, Ultrasonics, 54 (2014), 1281-1288.

[20] A. N. Lazaridi, V. F. Nesterenko, Observation of a new type of solitary waves in one-dimensional granular medium, J. Appl. Mech. Tech. Phys. , 26-3 (1985), 405-408.

[21] M. de Billy, A. C. Hladky-Hennion, On the formation of envelope solitons with tube ended by spherical beads, Ultrasonics, 52 (2012), 851-860.

[22] C. Coste, E. Falcon, S. Fauve, Solitary waves in a chain of beads under Hertz contact, Phys. Rev. E, 56-5 (1997), 6104–6117.

[23] C. Daraio, V. F. Nesterenko, E. B. Herbold, S. Jin, Tunability of solitary wave properties in one-dimensional strongly nonlinear phononic crystals, Phys. Rev. E, 73-2 (2006), 026610.

[24] M. Moleron, A. Leonard, C. Daraio, Solitary waves in chain of repelling magnets, J. Appl. Phys., 115 (2014), 184901.

[25] A. P. Chetverikov, W. Ebeling, M. G. Velarde, Localized nonlinear, soliton-like waves in two-dimensional anharmonic lattices, Wave Motion, 48 (2011), 753-760.

[26] H. Y. Hao, H. J. Maris, Experiments with acoustic solitons in crystalline solids, Phys. Rev. B, 64-6 (2001), 064302.

[27] P. Hess, A.M. Lomonosov, Solitary surface acoustic waves and bulk solitons in nanosecond and picosecond laser ultrasonics, Ultrasonics, 50 (2010), 167-171.

[28] S. V. Kuznetsov, Soliton-like lamb waves, J. Appl. Math. Mech., 73 (2009), 71-76.

[29] A. M. Lomonosov, P. Hess, Nonlinear surface acoustic waves: Realization of solitary pulses and fracture, Ultrasonics, 48 (2008), 482-487.

[30] A. P. Mayer, Nonlinear surface acoustic waves: Theory, Ultrasonics, 48 (2008), 478-481.

[31] A. S Kovalev, A. P. Mayer, C. Eckl, G. A. Maugin, Solitary Rayleigh waves in the presence of surface nonlinearities, Phys. Rev. E, 66-3 (2002), 036615.

[32] J. Engelbrecht, A. Berezovski, A. Salupere, Nonlinear deformation waves in solids and dispersion, Wave Motion, 44 (2007), 493-500.

[33] D. R. Christie, K. J. Muirhead, R. H. Clarke, Solitary waves in lower atmosphere, Nature, 293 (1981), 46-49.

[34] M. P. Rao, P. Castracane, S. Casadio, D. Fuà, G. Fiocco, Observations of atmospheric solitary waves in the urban boundary layer, Bound.-layer Meteor., 111 (2004), 85-108.

[35] R. J. Doviak, S. S. Chen, D. R. Christie, A thunderstorm-generated solitary wave observation compared with theory for nonlinear waves in a sheared atmosphere, J. Atmos. Sci., 48-1 (1991), 87-111.

[36] C. E. Synolakis, The run-up of solitary waves, J. Fluid Mech., 185 (1987), 523-545.

[37] Y. Li, F. Raichlen, Non-breaking and breaking solitary wave run-up, J. Fluid Mech., 456 (2002), 295-318.

[38] J. R. Apel, L. A. Ostrovsky, Y. A. Stepanyants, J. F. Lynch, Internal solitons in the ocean and their effect on underwater sound, J. Acoust. Soc. Am., 121-2 (2007), 695-722.

[39] N. Sugimoto, M. Masuda, J. Ohno, D. Motoi, Experimental demonstration of generation and propagation of acoustic solitary waves in a air-filled tube, Phys. Rev. Lett., 83-20 (1999), 4053-4056.

[40] N. Sugimoto, Propagation of nonlinear acoustic waves in a tunnel with an array of Helmholtz resonators, J. Fluid. Mech., 244 (1992), 55-78.

[41] N. Sugimoto, Acoustic solitary waves in a tunnel with an array of Helmholtz resonators, J. Acoust. Soc. Am., 99-4 (1996), 1971-1976.

[42] N. Sugimoto, M. Masuda, K. Yamashita, H. Horimoto, Verification of acoustic solitary waves, J. Fluid. Mech., 504 (2004), 271-299.

[43] B. Lombard, J.F. Mercier, Numerical modeling of nonlinear acoustic waves in a tube with Helmholtz resonators, J. Comput. Phys., 259 (2014), 421-443.

[44] A. Chaigne, J. Kergomard, Acoustique des Instruments de Musique, Belin (2008).

[45] M. F. Hamilton, D. T. Blackstock, Nonlinear Acoustics, Academic Press (1998).

[46] W. Chester, Resonant oscillations in closed tubes, J. Fluid Mech., 18 (1964), 44-64.

[47] P. Monkewitz, N. M. Nguyen-Vo, The response of Helmholtz resonators to external excitation. Part 1. Single resonators, J. Fluid Mech., 151 (1985), 477-497.

[48] P. Monkewitz, The response of Helmholtz resonators to external excitation. Part 2. Arrays of slit resonators, J. Fluid Mech., 156 (1985), 151-166.

[49] L. Menguy, J. Gilbert, Weakly nonlinear gas oscillations in air-filled tubes; solutions and experiments, Acta Acustica united with Acustica, 86-5 (2000), 798-810.

[50] I. Podlubny, Fractional Differential Equations, Academic Press (1999).

[51] N. Sugimoto, T. Horioka, Dispersion characteristics of sound waves in a tunnel with an array of Helmholtz resonators, J. Acoust. Soc. Am., 97-3 (1995), 1446-1459.

[52] O. Richoux, V. Pagneux, Acoustic characterization of the Hofstadter butterfly with resonant scatterers, Europhys. Lett., 59 (1) (2002), 34-40.

[53] K. Diethelm, An investigation of some nonclassical methods for the numerical approximation of Caputo-type fractional derivatives, Numer. Algor., 47 (2008), 361-390.

[54] A. Ben Jazia, B. Lombard, C. Bellis, Wave propagation in a fractional viscoelastic Andrade medium: Diffusive approximation and numerical modeling, Wave Motion, 51 (2014), 994-1010.

[55] F. Kappel, A. Kuntsevich, An implementation of Shor's r-algorithm, Comput. Optim. Appl., 15-2 (2000), 193-205.

[56] A. Rekik, R. Brenner, Optimization of the collocation inversion method for the linear viscoelastic homogenization, Mech. Res. Comm., 38 (2011), 305-308.

[57] N. Shor, Minimization Methods for Non-Differentiable Functions, Springer-Verlag (1985).

[58] C. Birk, C. Song, An improved non-classical method for the solution of fractional differential equations, Comput. Mech., 46 (2010), 721-734.

[59] E. F. Toro, Riemann Solvers and Numerical Methods for Fluid Dynamics. A Practical Introduction, Springer-Verlag (1999).

[60] R. J. LeVeque, Numerical methods for conservation laws, 2nd edition, Birkhäuser-Verlag (1992).

[61] N. Sugimoto, Burgers equation with a fractional derivative; hereditary effects on nonlinear acoustic waves, J. Fluid. Mech., 225 (1991), 631-653.